

Received 18 April 2023, accepted 13 May 2023, date of publication 17 May 2023, date of current version 25 May 2023.

Digital Object Identifier 10.1109/ACCESS.2023.3277388

RESEARCH ARTICLE

Performance Assessment of a RIS-Empowered Post-5G/6G Network Operating at the mmWave/THz Bands

VASCO R. J. VELEZ^{1,2}, JOÃO PEDRO C. B. B. PAVIA^{2,3},
NUNO M. B. SOUTO^{1,2}, (Senior Member, IEEE), PEDRO J. A. SEBASTIÃO^{1,2}, (Member, IEEE),
AND AMÉRICO M. C. CORREIA^{1,2}, (Senior Member, IEEE)

¹Department of Information Science and Technology, ISCTE—Instituto Universitário de Lisboa, 1649-026 Lisboa, Portugal

²Instituto de Telecomunicações, 1049-001 Lisboa, Portugal

³COPELABS, Universidade Lusófona, 1749-024 Lisboa, Portugal

Corresponding author: Vasco R. J. Velez (Vasco_vez@iscte-iul.pt)

This work was supported by FCT/MCTES through national funds and co-funded by EU funds under Project UIDB/50008/2020.

ABSTRACT Reconfigurable Intelligent Surfaces (RISs) are considered to be a key enabling technology for 6G as they can potentially provide a boost in performance with a high energy efficiency. RISs rely on the use of arrays with a large number of low-cost quasi-passive reflecting elements which can be individually tuned in order to shape the radio wave propagation. This can effectively enable the implementation of smart radio environments, increasing the capacity and improving the coverage of the system. Since most RISs related studies focus on evaluating the gains of RIS based solutions in simplified communication scenarios, in this paper we investigate the potential benefits of RISs when integrated into future wireless networks within the context of post-5G/6G systems. With this aim, we present an iterative algorithm for accomplishing the joint design of the access point precoder and phase-shifts of the RIS elements considering a multi-stream multiple-input multiple output (MIMO) orthogonal frequency division multiplexing (OFDM) link. Based on this approach, we then present the system-level evaluation of a RIS-aided post-5G/6G network deployment operating in two different bands, mmWave and sub-THz, and which considers both near-field and far-field propagation models. The results obtained in two different environments namely, Indoor Open Office (IOO) and Urban Micro Truncated (UMT), show that the adoption of the proposed RIS-based approach can effectively improve the throughput and coverage area.

INDEX TERMS Reconfigurable intelligent surfaces, MIMO, system level evaluation, mmWave, terahertz.

I. INTRODUCTION

In recent years, services based on mobile internet have grown exponentially in wireless cellular networks. The considerable increase in the number of connected devices requires the development of new strategies that are capable to improve the quality and reliability of mobile communications. This is an effort that has been enabling the research community to propose several novel solutions for future evolutions of wireless networks [1]. Increasing spectral and energy efficiency is a principle that is transverse to each generation of

mobile communications, whose basis started with multiplexing techniques (e.g. Orthogonal Frequency Division Multiplexing (OFDM) techniques), which were later on expanded with the spatial domain resorting to methods such as multiple input multiple output (MIMO) schemes. Recent improvements include index modulations which can explore the indexes of resource blocks to carry information, for example the spatial resources, frequency resources or even both, as in the case of generalized spatial-frequency index modulation (GSFIM) [2].

Recent studies have been documented in the literature which can potentially address some of the challenges that must be tackled in future sixth generation wireless networks

The associate editor coordinating the review of this manuscript and approving it for publication was Adao Silva¹.

(6G) [3]. One particular approach within the context of the physical layer encompasses reconfigurable intelligent surfaces (RIS) [4]. This new paradigm shift can potentially increase the quality of communication links in wireless communications [5]. The main idea underlying the use of RIS is the creation of smart environments which can improve wireless communications while also being able to target other type of applications such as location, sensing, and wireless power transfer [6]. Since networks are constantly developing towards a software-based solution, the notion of smart environments is not new.

RIS can be synthesized as an “intelligent” surface comprising a large set of periodic elements that can change the phase (and also the amplitude) of incident waves [7]. These structures are programmable, and they can be used to control electromagnetic wave propagation by generating constructive or destructive interference in the desired directions. Such feature allows us to improve the quality of the links between the transmitter and receiver. RIS may be attached to practically any surface, including walls, furniture, building panels, and clothes. Another advantage of this technology is that its operation is typically quasi-passive, making it a low complexity and energy efficient approach. Due to the low power consumption and the possibility to be embedded in surrounding objects, these surfaces can be seen as a cost-effective solution for future wireless networks [8]. One of the main objectives of using RIS aided systems is to extend the coverage of a wireless network. Considering this purpose, the authors in [9] analyzed the optimal location and orientation of a RIS in order to maximize the cell coverage when considering the communication from a BS to a single user. It was concluded that besides being located at a moderate distance from the BS, the RIS should be deployed vertically to the direction from the BS to the RIS. Although these types of surfaces can implement passive beamforming towards the receiver, they also work in full-duplex [4].

The large distance attenuation that takes place in the millimeter wave (mmWave) and Terahertz (THz) bands makes it difficult to achieve large coverage under the limitation of the maximum available base station (BS) transmit power. This phenomenon tends to worsen especially in systems designed for outdoor environments (even when considering highly directional antenna arrays). Another particular characteristic that is verified at mmWaves and THz bands is that the propagation channel tends to be spatially sparse, which results in a lower number of propagations paths. Such challenges can be coped with the aid of RISs, since these devices can operate as a centralized beamformer that can increase the channel gains. Moreover, RIS can also create additional propagation paths around major obstacles and enable line-of-sight (LOS) links to distant receivers [10].

In [11], the authors addressed an indoor scenario considering the use of RISs and the application of deep learning algorithms for maximizing the SNRs at the receivers. Their work focused on the design of a deep neural network that can provide the best received signal strength between users

and transmitters, with the aid of RIS panels. In [12] the authors studied a system operating at the THz band using a RIS for an indoor and outdoor scenario that optimizes the phase shifts of the individual elements in order to assist an ultra-massive MIMO (UM-MIMO) communication link. Performance results showed that the approach was capable of effectively extending the communication range. The authors in [13], developed an algorithm to calculate the ideal phases for each RIS element in order to maximize the capacity of the transmission. In their study, a MIMO-OFDM link with frequency-selective fading channel and perfect channel state information was considered. Promising gains were shown on high and low SNRs values.

According to the literature, due to their energy efficiency, RIS can be a viable alternative to traditional amplifiers and relays when considering multi-user communication scenarios, as demonstrated by the authors in [14]. The authors in [15] described a system with a single access point (AP) that distributes packets to several users. The system is able to improve the performance of both orthogonal multiple access (OMA) and non-orthogonal multiple access (NOMA) with the aid of RIS. Although, they considered only a single antenna for both transmitter and receiver, it was proved that RIS can enhance both the capacity and rate of the system. Nevertheless, point-to-point communications in MIMO systems aided by RIS are still a challenge.

Although some results obtained with test bench prototypes exist in the literature [16], [17], they all comprise small-scale configurations. Furthermore, the use of RIS-assisted systems combined with MIMO configurations in Cloud Radio Access Network (C-RAN) requires more in-depth research into the optimization process and overall impact. The authors in [18] considered a RIS-aided cellular network and also presented an algorithm for joint optimization of the active beamforming at the BS and passive beamforming of the RIS. Their simulation results showed some performance improvements against other existing algorithms. In [19], the authors presented one of the first system-level studies of a RIS-aided network deployment, using two frequencies of fifth generation new radio (5G NR) namely, the C-band (3.5GHz) and mmWave band (28GHz). While assuming a simplified operation in the far-field region with the RIS configured as anomalous reflectors, they demonstrated through a three-dimensional simulator how RISs can benefit a typical 5G urban network. Also, in [20], authors studied a system level design with an improved antenna model that analyses the pathloss, power and overall coverage between the transmitter and receiver with the aid of relayed RIS. Their results showed that the impact of the placement of RIS can affect the performance of the system, specially at edges of the sector cell. Despite the promising results of these initial studies, more research on the integration of RIS in future wireless networks is required before large-scale experimental deployments can become a reality. In fact, at the mm-Wave or THz frequencies, the distances between BSs will tend to be short enabling users to be connected to more than one BS simultaneously. Therefore,

it is important to study whether RIS panels integrated into these Micro/Pico cells can effectively increase the coverage area as well as the throughput within the context of mmWave/THz networks in post-5G/6G RAN.

Motivated by the above work, in this paper we study the integration of RIS-assisted MIMO communications operating in mmWave/sub-THz bands into future post-5G/6G networks. Considering this objective, we first present an algorithm for joint precoding and RIS optimization which is then used as a basis for the system-level evaluation of a post-5G/6G RAN operating with multiple APs/BSSs, multiple RIS panels and multiple users. Several numerical evaluations are presented and analyzed under different configurations, which demonstrate the effectiveness of the proposed optimization algorithm and the beneficial impact of the RISs. The main contributions of this paper can be summarized as follows:

- Targeting scenarios where the communication for different users is based on orthogonal multiple access, we propose a new algorithm that jointly computes the precoder and the phase shifts of RIS panels placed in between the receiver and the transmitter. Such strategy aims to maximize the achievable rate in a multicarrier point-to-point MIMO communication. The proposed algorithm uses the alternating maximization (AM) method to decouple the optimization variables and split the main problem into two simpler ones. The first subproblem is then solved using the singular value decomposition (SVD) combined with water filling whereas the second one is addressed with the accelerated proximal gradient (APG) approach. We refer to the resulting algorithm as AM-SVD-APG;
- We integrated the proposed RIS aided scheme into a post-5G/6G RAN based on MIMO-OFDM which operates at the mmWave and sub-THz bands and considered numerologies 3 and 5 of 5G New Radio in order to perform a thorough system level assessment. For this assessment, both near-field and far-field propagation models were considered.
- A thorough system level evaluation was presented and analyzed for two main scenarios of 5G NR. The first scenario was set for mmWave (28GHz), and considered an Urban Micro Truncated (UMT) environment where several BSs transmit to multiple receivers with the aid of RIS panels placed around the cells. The second scenario was set for sub-THz (100GHz) and considered a deployment in an indoor environment surrounded by obstacles (Indoor Open Office - IOO). Results show that the throughput and coverage area of a post-5G/6G RAN can effectively improve, when integrating the proposed RIS-based approach.

The paper is organized as follows: Section II presents the system model for the RIS-assisted MIMO-OFDM system. Section III derives the joint precoding and RIS design algorithm followed by the description of the evaluated system-level scenarios in section IV. Performance results

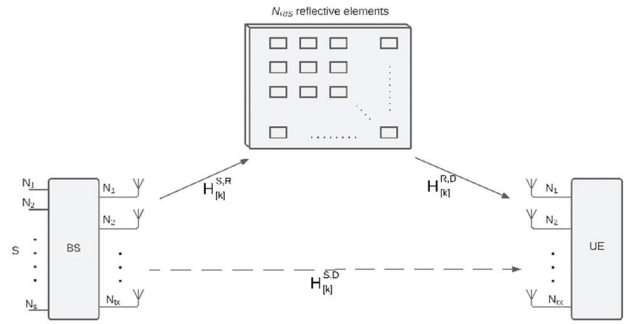


FIGURE 1. Example of a MIMO-OFDM communication system aided by RIS, consisting of BS, UE, and RIS panel with N_{RIS} reflecting elements.

are then presented and analyzed in section V. Finally, the conclusions are outlined in section VI.

Notation: Bold lower and upper-case letters represent vectors and matrices, respectively. $\mathbb{C}^{a \times b}$ denotes the space of complex matrices of dimensions $a \times b$, $(\cdot)^H$ denotes the conjugate transpose of a matrix/vector, $\|\cdot\|_F$ is the Frobenius norm of a matrix, $diag(\mathbf{a})$ is a diagonal matrix with elements of \mathbf{a} on its diagonal, and \mathbf{I}_n is the $n \times n$ identity matrix.

II. SYSTEM MODEL

Targeting practical scenarios where the communication for different users is based on orthogonal multiple access, as for example in orthogonal frequency division multiple access (OFDMA), let us consider the downlink connection of a point-to-point MIMO communication system operating at the mmWave/THz band, as illustrated in Figure 1. In this figure, we observe an AP/BS with an array of N_{tx} antennas transmitting to a user equipment (UE) with N_{rx} antennas, with the aid of a RIS panel with N_{RIS} elements. It is assumed that the system adopts OFDM to cope with frequency selective fading. In this study we essentially consider two scenarios. The first scenario is based on an outdoor environment in which a BS serves several users, with different carrier frequency and distance pathways than those discussed in the second scenario. The second scenario, on the other hand, is based on indoor environment, in which surrounding obstacles can easily block or obstruct the communication link. Such fact presents itself as critical especially in cases where direct LOS is used, or when the signal suffers attenuation losses. Both cases can be assisted with RIS panels with N_{RIS} reflective elements each with the purpose of improving communication links.

Every transmission comprises up to N_s simultaneous data streams per subcarrier k , which are represented as $\mathbf{s}[k] = [s_{1,k} \dots s_{N_s,N_c}]^T$, where $s_{i,k} \in \mathbb{C}$ corresponds to an amplitude and phase modulated symbol with $E[\|\mathbf{s}[k]\|^2] = N_s$. Using a baseband representation, the signal arriving at a user at each subcarrier k , $\mathbf{R}[k] \in \mathbb{C}^{N_s \times 1}$, can be modeled after the combiner as

$$\mathbf{R}[k] = \sqrt{\rho} \mathbf{W}[k]^H \mathbf{H}[k] \mathbf{F}[k] \mathbf{s}[k] + \mathbf{W}[k]^H \mathbf{n}[k], \quad (1)$$

where $k = 1, \dots, N_c$, N_c is the total number of subcarriers allocated to the target user, ρ denotes the power per stream and per subcarrier, $\mathbf{W}[k] \in \mathbb{C}^{N_{rx} \times N_s}$ is the user combining matrix, $\mathbf{H}[k] \in \mathbb{C}^{N_{rx} \times N_{tx}}$ is the overall frequency domain channel matrix between the BS/AP and user, which includes the paths through the RIS panel, $\mathbf{F}[k] \in \mathbb{C}^{N_{tx} \times N_s}$ is the BS precoder matrix, $\mathbf{s}[k] \in \mathbb{C}^{N_s \times 1}$ is the vector of symbols and $\mathbf{n}[k] \in \mathbb{C}^{N_{rx} \times 1}$ is the noise vector whose elements follow an independent zero mean circularly symmetric Gaussian distribution with covariance $\sigma_n^2 \mathbf{I}_{N_{rx}}$. The total channel matrix $\mathbf{H}[k]$ can be represented as

$$\mathbf{H}[k] = \mathbf{H}[k]^{S,D} + \mathbf{H}[k]^{R,D} \Phi \mathbf{H}[k]^{S,R}, \quad (2)$$

where, $\mathbf{H}[k]^{S,D} \in \mathbb{C}^{N_{rx} \times N_{tx}}$ is the channel between the BS/AP and the user, $\mathbf{H}[k]^{R,D} \in \mathbb{C}^{N_{rx} \times N_{RIS}}$ is the channel between the RIS panel and user, $\Phi \in \mathbb{C}^{N_{ris} \times N_{ris}}$ is the matrix that models the effect of the RIS elements, having a diagonal structure with $\Phi = \text{diag}(\boldsymbol{\varphi})$, where $\boldsymbol{\varphi} = [\varphi_1, \dots, \varphi_{N_{ris}}]^T$ and φ_m denotes the phase shift of the m^{th} element of the RIS, and $\mathbf{H}[k]^{S,R} \in \mathbb{C}^{N_{RIS} \times N_{tx}}$ is the channel between the BS/AP and the RIS panel.

III. JOINT PRECODING AND RIS OPTIMIZATION

After introducing the system model in the previous section, we present the problem formulation which aims at maximizing the achievable rate in a MIMO-OFDM communication link aided by RIS panels. Considering a total of N_f subcarriers (with N_c subcarriers allocated to the target user), a cyclic prefix length of N_{CP} and assuming perfect channel knowledge, then the achievable rate in bits/s/Hz for the user is given by [13]

$$R = \frac{N_f}{(N_f + N_{CP}) N_c} \sum_{k=1}^{N_c} \log_2 \det \left(\mathbf{I}_{N_s} + \frac{\rho}{P_n} \mathbf{F}[k]^H \mathbf{H}[k]^H \mathbf{H}[k] \mathbf{F}[k] \right) \times \mathbf{H}[k] \mathbf{F}[k]. \quad (3)$$

Defining the power constraint at each subcarrier as $\|\mathbf{F}[k]\|_F^2 \leq N_s$ (which results in a total effective transmitted power of $P_{user} = \rho N_s N_c$ for that user) and assuming that the RIS panel only allows tuning the phase shifts of the individual reflecting elements, with this tuning being the same at all subcarriers, then we can formulate the problem as

$$\begin{aligned} \min_{\substack{\mathbf{F}[k] \in \mathbb{C}^{N_{tx} \times N_s} \\ \boldsymbol{\varphi} \in \mathbb{C}^{N_{ris} \times 1}}} f(\mathbf{F}[k], \boldsymbol{\varphi}) &= - \sum_{k=1}^{N_c} \ln \det \\ &\times \left(\mathbf{I}_{N_s} + \frac{\rho}{P_n} \mathbf{F}[k]^H \times \mathbf{H}[k]^H \mathbf{H}[k] \mathbf{F}[k] \right) \\ \text{subject to } \|\mathbf{F}[k]\|_F^2 &\leq N_s \\ |\varphi_i| &= a, \quad i = 1, \dots, N_{RIS}, \end{aligned} \quad (4)$$

where $\mathbf{F}[k] \in \mathbb{C}^{N_{tx} \times N_s}$ is the BS/AP precoder matrix, P_n denotes the noise power in each sub-band ($P_n = \sigma_n^2$), and a is the amplitude of each reflection element in the RIS. It is

TABLE 1. Algorithm 1: am-svd-app.

ALGORITHM 1: AM-SVD-APG	
1:	Input: $\mathbf{R}[k], \mathbf{H}[k], Q, \boldsymbol{\varphi}^{(0)}$
2:	For $q = 1, \dots, Q$ do
3:	$\mathbf{F}[k] = \mathbf{V}_{:,1:N_s}[k] \mathbf{D}[k], \quad k = 1, \dots, N_c$
4:	$\mathbf{y}^{(q)} = \boldsymbol{\varphi}^{(q)} + \frac{q}{q+3} (\boldsymbol{\varphi}^{(q)} - \boldsymbol{\varphi}^{(q-1)})$
5:	$\boldsymbol{\varphi}^{(q+1)} = (\mathbf{y}^{(q)} - \alpha \nabla f(\mathbf{y}^{(q)})) \oslash [\mathbf{y}^{(q)} - \alpha \nabla f(\mathbf{y}^{(q)})]$
6:	End for
7:	Output: $\mathbf{F}[k], \boldsymbol{\varphi}, \quad k = 1, \dots, N_c$

important to note that the constants present in the achievable rate expression (3) were dropped in the definition of the objective function $f(\mathbf{F}[k], \boldsymbol{\varphi})$ and that the combiner is not part of the adopted optimization problem.

To solve problem (4), first we use the AM method, in order to decouple the optimization variables and simplify the problem. This approach allows problem (4) to be split into two subproblems which are simpler to address. The first subproblem is defined by fixing $\boldsymbol{\varphi}$ in (4) and then solving over $\mathbf{F}[k]$, which results in the following formulation

$$\begin{aligned} \min_{\mathbf{F}[k] \in \mathbb{C}^{N_{tx} \times N_s}} &- \sum_{k=1}^{N_c} \ln \det \left(\mathbf{I}_{N_s} + \frac{\rho}{P_n} \mathbf{F}[k]^H \mathbf{H}[k]^H \mathbf{H}[k] \mathbf{F}[k] \right) \\ \text{s.t. } &\|\mathbf{F}[k]\|_F^2 \leq N_s. \end{aligned} \quad (5)$$

This problem can be solved using the SVD combined with a water filling algorithm [21], [22]. The SVD of the channel matrix at subcarrier k can be written as

$$\mathbf{H}[k] = \mathbf{U}[k] \boldsymbol{\Lambda}[k] \mathbf{V}[k], \quad (6)$$

where $\mathbf{U}[k]$ is the matrix with left singular vectors, $\boldsymbol{\Lambda}[k]$ is the diagonal matrix with the singular values in decreasing order, and $\mathbf{V}[k]$ is the matrix containing the right singular vectors. The precoder matrix is then set as $\mathbf{F}[k] = \mathbf{V}_{:,1:N_s}[k] \mathbf{D}[k]$, where $\mathbf{D}[k] = \text{diag}(d_1, \dots, d_{N_s})$ is obtained using a water-filling algorithm applied to the singular values of $\mathbf{H}[k]$, (that is, to the diagonal of $\boldsymbol{\Lambda}[k]$) with a total allocated power of N_s .

The second subproblem corresponds to minimizing (4) over $\boldsymbol{\varphi}$, with the precoder matrices $\mathbf{F}[k]$ ($k = 1, \dots, N_c$) fixed and can be rewritten as

$$\begin{aligned} \min_{\boldsymbol{\varphi} \in \mathbb{C}^{N_{ris} \times 1}} &- \sum_{k=1}^{N_c} \ln \det \left(\mathbf{I}_{N_s} + \frac{\rho}{P_n} \mathbf{F}[k]^H \mathbf{H}[k]^H \mathbf{H}[k] \mathbf{F}[k] \right) \\ &+ I_{|\varphi|=a}(\boldsymbol{\varphi}), \end{aligned} \quad (7)$$

where $I_{|\varphi|=a}(\boldsymbol{\varphi})$ is the set indicator function which returns zero if $|\varphi_i| = a$ for any $i = 1, \dots, N_{RIS}$, and returns $+\infty$ otherwise. The use of the indicator function allows us to incorporate the RIS phase shifts constraint defined in (3) directly into the objective function, thus resulting in an unconstrained optimization problem. To address the optimization problem in (7)

which is nonconvex and difficult to solve due to the constant amplitude phase-shift constraint, we apply an APG method [23]. This method relies on iteratively applying a gradient-based step, followed by a proximal mapping. In order to improve the typical slow convergence of proximal gradient methods [24], the APG method computes the gradient step over an extrapolated point, which is a linear combination of the previous two estimates. Therefore, in the proposed approach we adopt the extrapolated variable defined as

$$\mathbf{y}^{(q)} = \boldsymbol{\varphi}^{(q)} + \frac{q}{q+3} \left(\boldsymbol{\varphi}^{(q)} - \boldsymbol{\varphi}^{(q-1)} \right), \quad (8)$$

where q is the iteration number and $q/(q+3)$ corresponds to the extrapolation parameter (as suggested in [23]). The algorithm will thus consist of iteratively updating the estimate $\boldsymbol{\varphi}^{(q+1)}$, by applying the proximal operator to a gradient step over $\mathbf{y}^{(q)}$, namely

$$\boldsymbol{\varphi}^{(q+1)} = \text{prox}_{\alpha \mathbf{I}_{|\varphi|=a}} \left(\mathbf{y}^{(q)} - \alpha^{(q)} \nabla f \left(\mathbf{y}^{(q)} \right) \right), \quad (9)$$

with $\alpha^{(q)}$ denoting the step size (can be found through backtracking line search [23]). The proximal operator for a function g is defined as $\text{prox}_g(\mathbf{z}) = \underset{\hat{\mathbf{x}}}{\text{argmin}} g(\hat{\mathbf{x}}) + \frac{1}{2} \|\hat{\mathbf{x}} - \mathbf{z}\|^2$ which for (9), can be calculated as the projection over the set of vectors whose elements have modulus to equal a . Therefore, we can rewrite (9) as

$$\boldsymbol{\varphi}^{(q+1)} = \left(\mathbf{y}^{(q)} - \alpha^{(q)} \nabla f \left(\mathbf{y}^{(q)} \right) \right) \oslash \left[\mathbf{y}^{(q)} - \alpha^{(q)} \nabla f \left(\mathbf{y}^{(q)} \right) \right], \quad (10)$$

where \oslash denotes the Hadamard division. The gradient of $f(\mathbf{y})$ can be computed using (the details of the derivation are presented in Appendix)

$$\begin{aligned} \nabla f \left(\mathbf{y}^{(q)} \right) = & -\frac{\rho}{P_n} \sum_{k=1}^{N_c} \text{diag} \left[\left(\mathbf{H}[k]^{R,D} \right)^H \mathbf{H}[k] \mathbf{F}[k] \right. \\ & \times \left(\mathbf{I}_{N_s} + \frac{\rho}{P_n} \mathbf{F}[k]^H \mathbf{H}[k]^H \mathbf{H}[k] \mathbf{F}[k] \right)^{-1} \\ & \left. \times \mathbf{F}[k]^H \left(\mathbf{H}[k]^{S,R} \right)^H \right]. \end{aligned} \quad (11)$$

Table 1, summarizes all steps of the proposed joint precoding and RIS optimization algorithm, which we refer to as AM-SVD-APG.

Regarding the complexity, the proposed algorithm of AM-SVD-APG mainly involves the SVD computations in step 3 as well as some matrix/vector multiplications and a small matrix inversion in step 5. It can be seen that this results in an overall computational complexity order of $\mathcal{O} \left(QN_c \left(N_{tx}N_{rx}N_{ris} + N_{tx}N_{rx}^2 + N_{rx}^3 \right) \right)$. For comparison, the APG algorithm in [12] has a complexity order of $\mathcal{O} \left(N_cN_{tx}N_{rx}^2 + N_cQ \left(N_{tx}N_{rx}N_{ris} + N_{rx}^3 + N_{rx}^2N_{ris} + N_sN_{tx} \times N_{rx} \right) \right)$ and the projected gradient method (PGM) algorithm from [32] has a complexity of $\mathcal{O} \left(Q \left(N_{rx}^3 + N_{rx}^2N_{tx} + N_{rx}N_{tx}^2 + N_{rx}N_{tx}N_{ris} + N_{tx}^3 \right) \right)$ (it is important to note that PGM does not consider multicarrier

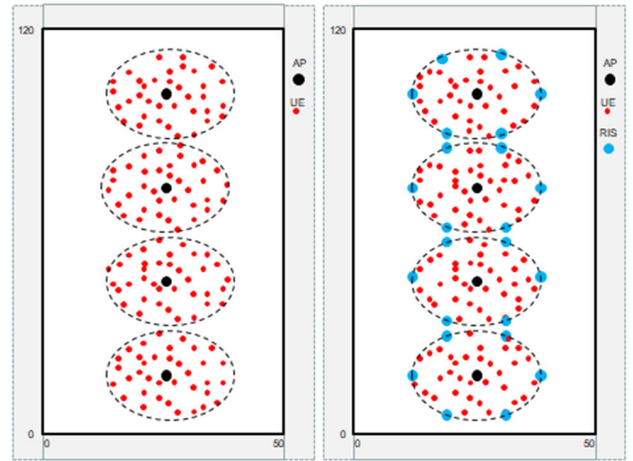


FIGURE 2. IOO environment where black dots are represented as AP, and blue dots RIS panels. Users are shown in red dots that are dispersed in random positions across the floor. IOO scenario without RIS (left) and with RIS assistance (right).

transmissions). While the complexity of AM-SVD-APG algorithm has a strong dependency on the receiver array size due to the SVD that is calculated in all iterations, in a typical downlink scenario the receiver array is much smaller than that of the transmitter array and RIS panel. Therefore, the complexity growth of AM-SVD-APG and APG is mainly caused by the product of these three dimensions weighted by the number of sub-carriers and iterations, namely $\mathcal{O} \left(QN_cN_{tx}N_{rx}N_{ris} \right)$. As for PGM, it also grows with the product of these dimensions as well as with $\mathcal{O} \left(QN_{tx}^3 \right)$.

IV. SYSTEM-LEVEL CONFIGURATION AND SCENARIOS

After presenting the signal model for the individual links between BS and user as well as the proposed joint precoding and RIS design algorithm, in this section we describe the setup adopted for the post-5G/6G RAN system level assessment, detailing the target scenarios that were evaluated. The considered scenarios are based on two modified 3GPP environments [25]: the IOO environment, which corresponds to a traditional office space, and the UMT, which corresponds to a truncated Urban Micro Outdoor environment, that is based on urban micro dense areas.

The IOO scenario focuses on high user density inside buildings with offices that have indoor obstacles, such as walls and corridors. This scenario assumes that common offices have areas around $120 \times 50 \text{ m}^2$, as illustrated in Figure 2. In this case we considered sub-THz links with a carrier frequency of $f_c=100\text{GHz}$, and the bandwidth is $B = 0.4 \text{ GHz}$. UEs are uniformly placed, with a minimum distance of 1 meter around APs and RIS. The red dots on Figure 2 show the UEs settled on the scenario. The UEs are randomly and uniformly placed in each scenario at a given distance and angle from the APs or from the associated RIS panel. Depending on the distance, there is a probability of having a LOS and NLOS links. In the case of the NLOS links, it was also considered fading due to multipath following a Rayleigh

distribution with shadowing effect according to a Lognormal distribution. All parameters and equations are described in Tables 7.4.1-1 and 7.4.2-1 of [25].

A maximum of two UEs can be served simultaneously by each RIS panel, with the maximum distance between RIS and each UE being 7 m. The panels are represented as the bigger blue dots in Figure 2. On the APs side, they are represented as black dots, and they can support up to 14 UEs associated to each one. The maximum distance between AP and UEs is 17 m. For each AP placed, there are 6 nearest RIS panels coupled to that AP. The maximum distance between AP and RIS panels, is 17 m. For comparison purposes, we also simulated the same scenario, but without any influence of RIS panels, as shown on the left side of Figure 2.

The UMT scenario illustrated in Figure 3, focuses on micro cells with high user densities. This represents cases of high traffic loads in city centers with dense indoor areas. According to the scenario specifications, it has a truncated area of $470 \times 400 \text{ m}^2$. In our study, the operating frequency was set to $f_c=28\text{GHz}$ and the bandwidth to $B = 0.4 \text{ GHz}$. The Inter Site Distance (ISD) of UMT scenario is 200 m. UEs are also uniformly placed with a minimum distance of 1 meter around their respective BSs and RIS panels. The distribution of UEs across the scenario was based on the same spatial distribution of UEs described before for the previous scenario. The maximum distance between each UE and the associated BS is up to 89 m. Three different configurations were considered for the UMT scenario. In first one, each BS can accommodate up to 25 UEs, and does not have any aid from RISs, as shown on the top image of Figure 3. In the second configuration, almost all RIS panels were placed at 85 m from the nearest BS and the maximum distance between each UE and the corresponding RIS panel is 18 m. Up to two UEs can be linked to each corresponding RIS panel with a total of 20 RIS and 4 BS deployed. On average there are 5 RIS inside each BS coverage area, as represented in the middle image of Figure 3. In the third configuration the RIS panels are placed at 67 m (north and south sides), 58 m (left and right sides) or 88 m (diagonally) from the nearest BS, as displayed on bottom image of Figure 3. In this last deployment, there are 26 RIS panels and 4 BS which means that on average there are 6.5 RIS linked to each BS coverage area. This alternative setup manages to be more realistic, because RIS panels are placed at different distances. We must consider that it may not be always possible to place all RIS panels at exactly the same distance from the BSs, in a realistic deployment.

We consider that each RIS panel can be divided into small panels (called sub-panels), with N_{RIS} corresponding then to the number of elements in each sub-panel. This can be seen in Figure 4 where RISs are integrated into a hexagonal grid on the right size of same figure.

The total power transmitted by each AP at 100 GHz is set to 100mW (20dBm) for the IOO scenario, whereas 3.16W (35dBm) are transmitted from each BS at 28 GHz, in the case of the UMT scenario, see Table 7.8.1 of [25]. To serve the UEs, two types of links are considered namely a direct link

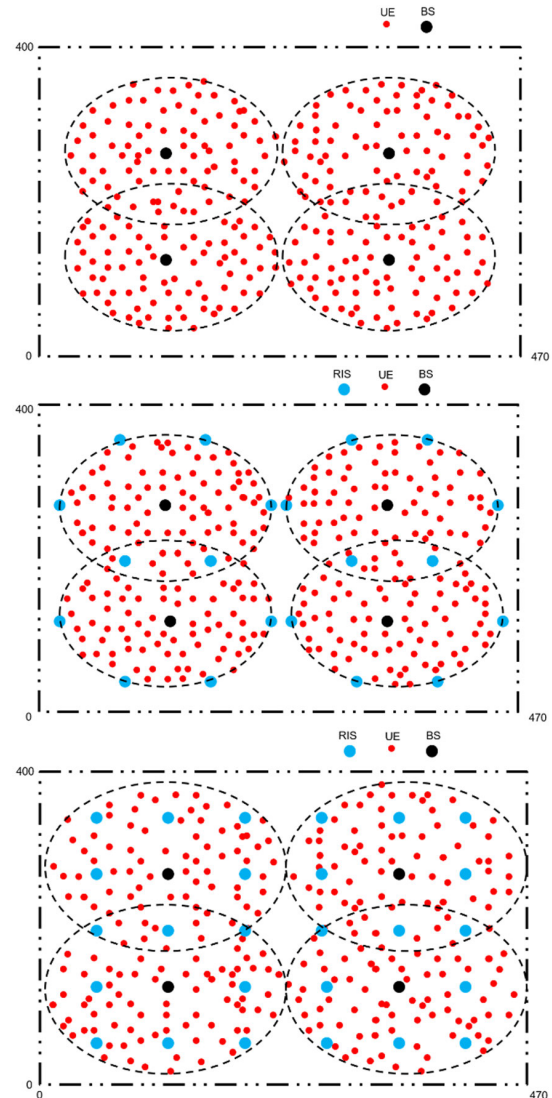


FIGURE 3. UMT scenario, without RIS (top image), with RIS placed at the same distance from the nearest BS (middle image) and with RIS placed at different distances of BS (bottom one).

between BS/AP and UE and an indirect link through the RIS. In the IOO case, due to the high attenuation at the sub-THz band for NLOS, it is assumed that there is only a direct link or only an indirect link, which is represented as 1C. For the UMT case there are double-links, where UEs are served simultaneously by a RIS and BS, which corresponds to 2C. The noise power is $N_0=-88 \text{ dBm}$ for the bandwidth $B = 0.4 \text{ GHz}$. The spacing between each element of the RIS panel is $d_{RIS} = \lambda/2=5.4 \text{ mm}$ (28GHz) and $d_{RIS}=1.5 \text{ mm}$ (100GHz), resulting in an area of $A=5.4^2=29.16 \text{ mm}^2$ and $A=2.25 \text{ mm}^2$ per element. The gains of the individual antenna elements of the arrays are 0 dBi for both the transmitter and receiver. Table 2 summarizes the parameters used in our two scenarios.

V. NUMERICAL RESULTS

In this section, we start by presenting the performance of the proposed algorithm AM-SVD-APG using link-level simulations and then extend the evaluation to system level

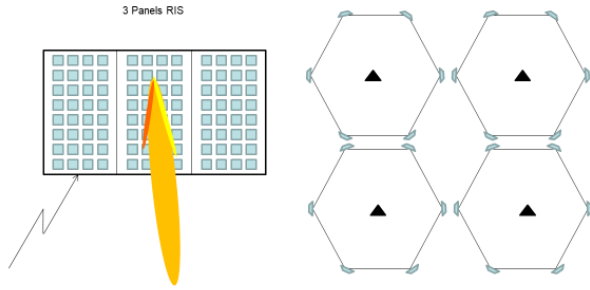


FIGURE 4. Example of RIS Panel with 3 sub-panels used in all simulated environments (left), and a hexagonal grid where 4 BS are located in the center (right).

TABLE 2. Parameters of simulated scenarios.

Parameters	IOO	UMT
Area (m ²)	120x50 m ²	470x400 m ²
Carrier Frequency	100 GHz	28 GHz
Cell Range	w/o RIS	10 m
	w/ RIS	17 m
UE mobility	3 km/h	3 km/h
UE distribution (horizontal)	Uniform	Uniform
Maximum UEs attached/sector	Up to 14	Up to 25
Transmit Power	20 dBm	35 dBm
AP/BS Gains	0 dBi	0 dBi
Area of RIS elements	2.25 mm ²	29.46 mm ²

considering the integration into a post-5G/6G RAN. In our evaluation, we assume that the channels can have a LOS component and N_{ray} NLOS paths. For the case when the RIS is located far from the transmitter, i.e., when the distance between them, $d^{S,R}$, is larger than the Fraunhofer distance defined as $D_F \triangleq 2L_{array}^2/\lambda$ [26] (L_{array} is the largest dimension of the array), we assume a far-field propagation model with planar wavefronts and express the channel frequency response between the AP and RIS as

$$\begin{aligned} \mathbf{H}[k]^{S,R} &= \sqrt{\beta_{LOS}^{S,R}} e^{-j2\pi \frac{d^{S,R}}{\lambda}} \mathbf{a}_R(\phi_0^{R \leftarrow S}, \theta_0^{R \leftarrow S}) \\ &\quad \times \mathbf{a}_S^H(\phi_0^{S \rightarrow R}, \theta_0^{S \rightarrow R}) \\ &\quad + \left(\sqrt{\frac{\beta_{NLOS}^{S,R}}{K_{Rice}}} \sum_{l=1}^{N_{ray}} \alpha_l^{S,R} \mathbf{a}_R(\phi_l^{R \leftarrow S}, \theta_l^{R \leftarrow S}) \right. \\ &\quad \left. \times \mathbf{a}_S^H(\phi_l^{S \rightarrow R}, \theta_l^{S \rightarrow R}) e^{-j2\pi \tau_l f_k} \right), \end{aligned} \quad (12)$$

where $f_k = f_c + \frac{B}{N_c} \left(k - 1 - \frac{N_c - 1}{2} \right)$, B is the bandwidth, f_c is the carrier frequency, τ_l is the delay of path l and K_{rice} specifies the ratio between the LOS and NLOS components. The coefficients $\alpha_l^{S,R}$ represent the complex gains of the NLOS rays, $\beta_{LOS}^{S,R}$ is the path loss of the LOS path and $\beta_{NLOS}^{S,R}$ denotes the path loss of the NLOS channel. This path loss can be approximated as [27]

$$\beta_{NLOS}^{S,R} = \frac{G_{Tx} A_R}{4\pi (d_{S \leftrightarrow R})^2} e^{-k_{abs}(f) d_{S \leftrightarrow R}}. \quad (13)$$

where G_{Tx} is the transmit antenna gain, A_R is the RIS element area, $k_{abs}(f)$ is the molecular absorption coefficient at

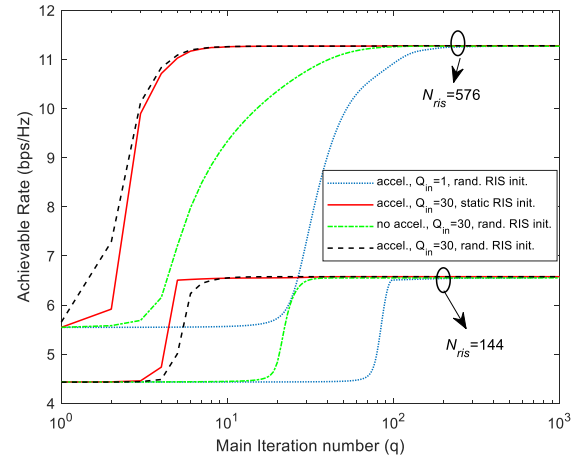


FIGURE 5. Achievable rate versus iterations number obtained with the proposed AM-SVD-APG for a scenario with $f=28\text{GHz}$, $N_{tx}=64$, $N_s=3$, $N_{rx}=16$, and $N_c=1$.

frequency f [28], and $d_{S \rightarrow R}$ is the distance/length between the transmitter (source) and the RIS panel (RIS).

The vectors $\mathbf{a}_R(\phi_l^{R \leftarrow S}, \theta_l^{R \leftarrow S})$ and $\mathbf{a}_S(\phi_l^{S \rightarrow R}, \theta_l^{S \rightarrow R})$, denote the RIS and transmitter array response vectors at the (azimuth, elevation) angles of $(\phi_l^{R \leftarrow S}, \theta_l^{R \leftarrow S})$ and $(\phi_l^{S \rightarrow R}, \theta_l^{S \rightarrow R})$, respectively. If a uniform planar array (UPA) is adopted, then the steering vector for the transmitter can be written as [29]

$$\begin{aligned} \mathbf{a}_S(\phi_l^{S \rightarrow R}, \theta_l^{S \rightarrow R}) &= \left[1, \dots, e^{j \frac{2\pi}{\lambda} d_{ant} (p \sin \phi_l^{S \rightarrow R} \sin \theta_l^{S \rightarrow R} + q \cos \theta_l^{S \rightarrow R})}, \dots \right. \\ &\quad \left. \dots, e^{j \frac{2\pi}{\lambda} d_{ant} ((\sqrt{N_{tx}} - 1) \sin \phi_l^{S \rightarrow R} \sin \theta_l^{S \rightarrow R} + (\sqrt{N_{tx}} - 1) \cos \theta_l^{S \rightarrow R})} \right]^T, \end{aligned} \quad (14)$$

where $p, q = 0, \dots, \sqrt{N_{tx}} - 1$ are the indices of the respective antennas, λ is the wavelength and d_{ant} is the inter-element spacing. The steering vectors can also be described using a similar notation for both $\mathbf{a}_R(\phi_l^{R \leftarrow S}, \theta_l^{R \leftarrow S})$ and $\mathbf{a}_D(\phi_l^{D \leftarrow S}, \theta_l^{D \leftarrow S})$. In the case when the distance between the RIS and the transmitter is smaller than the Fraunhofer distance we assume a near-field propagation model with spherical wavefronts. In this case the expression in (12) must include the effect of the distances of the paths between each individual transmit antenna element and each RIS element [30]. Regarding the other channels, namely $\mathbf{H}[k]^{R,D}$ and $\mathbf{H}[k]^{S,D}$, we adopt the same model, and thus they can also be expressed similarly to (12) (for the far field case).

A. LINK LEVEL EVALUATION

Regarding the link level evaluation, the results are presented in terms of bit error rate (BER) and measure the single-link performance between the transmitter and the user, considering the cases of no RIS and of RIS-aided communication. Whereas the precoder and RIS phases shifts are computed according to Algorithm I, for the combiner we apply a minimum mean squared error (MMSE) based equalizer computed

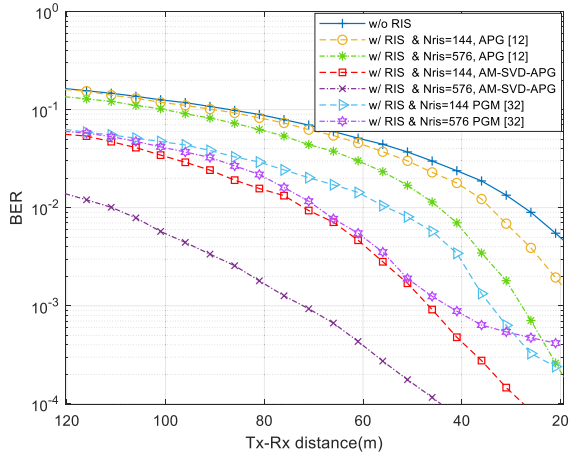


FIGURE 6. BER Comparison versus horizontal distance for a scenario with $f=28\text{GHz}$, $N_{tx}=64$, $N_s=3$, $N_{rx}=16$, $N_{ris}=144$ or 576 elements with $N_c=1$, where RIS panel is placed at a fixed position of $(20\text{m}, 8\text{m})$ and the user position changes between the receiver (RX) and the transmitter (TX).

using the equivalent channel as

$$\mathbf{W}^H[k] = \left(\mathbf{H}[k] \mathbf{F}[k] \right)^H \mathbf{H}[k] \mathbf{F}[k] + \frac{\rho}{P_n} \mathbf{I}_{N_s} \Big)^{-1} \times \mathbf{H}[k] \mathbf{F}[k]^H. \quad (15)$$

The assessment of the RIS optimization algorithm was performed through Monte Carlo simulations for different types of configurations, in a RIS assisted OFDM-MIMO system that operates both in IOO and UMT scenarios. The coordinates of the AP/BS and User are $(0\text{ m}, 0\text{ m})$, and $(1\text{ m to } d, 0\text{ m})$, respectively. Each variation of parameter d along the simulations, corresponds to changing the distance between the receiver and the transmitter (which will also affect the distance between the UE and the RIS panel).

The subcarrier spacing (SCS), transmission time interval (TTI), cyclic prefix (CP), and the number of symbols per slot, are all defined by the proposed 5G NR scalable OFDM numerology [31]. Our UMT and IOO scenarios were simulated considering the numerologies 3 and 5, respectively. In each scenario, we considered antenna arrays with $N_{tx} = 64$ up to 256 elements at the transmitter side. The receiver side has the same number of antennas namely, $N_{rx} = 16$, in all simulations. Different numbers of transmitted symbols per subcarrier were considered in the simulations, ranging from $N_s=1$ up to $N_s=3$. The number of OFDM subcarriers (N_c) used in the evaluations is $N_c = 60, 120, 132$ or 180 . All these numbers are multiples of 12, which corresponds to the number of subcarriers of a physical resource block in 5G NR [31].

To evaluate the convergence behavior of the proposed AM-SVD-APG algorithm as well as the effect of the initialization, Figure 5 present the achievable rate versus the iteration number, considering the UMT scenario with the following parameters: $N_{tx}=64$, $N_s=3$, $N_{rx}=16$ and $N_c=1$. The RIS panel is located at $(50\text{ m}, 5\text{ m})$ and the user at $(55\text{ m}, 0\text{ m})$. In the figure we define Q_{in} as the number of times steps 4 and 5 of the algorithm are repeated inside each main iteration.

The term ‘*accel*’ is used in the legend when we refer to the algorithm working with the extrapolated variable, as defined in (8). In the ‘*no accel*’ case, the algorithm does not work with the extrapolated variable when updating the phases of the RIS elements, in other words we set the extrapolation parameter to 0 and (8) reduces to $\mathbf{y}^{(q)} = \boldsymbol{\varphi}^{(q)}$. We can observe that the accelerated algorithm takes less than 10 main iterations to converge if steps 4 and 5 of the algorithm are repeated several times inside each main iteration ($Q_{in}=30$). This is a consequence of the fact that steps 4 and 5 implement an inner iterative method for providing an estimate for the solution of subproblem (7). Therefore, repeating them several times potentially provides a better solution for the RIS phases before proceeding to the following main iteration and attempt to solve subproblem (5) in step 3 to obtain an updated precoder matrix. It is important to note however, that this fast convergence happens only when using the extrapolation step (accelerated version of AM-SVD-APG) since the non-accelerated algorithm with $Q_{in}=30$ requires at least 50-100 main iterations to converge. Furthermore, it can also be observed that different initializations for the RIS, such as the static RIS with all the elements set as $\varphi_i=1$ (simple reflector), or a random initialization of the phases, do not seem to impact the final solution, resulting only in minor variations on the number of required iterations for the algorithm to converge.

Figure 6 shows the BER performance versus the distance for the individual link between the transmitter and a UE. For this comparison we use a power of $P_{user}=35\text{dBm}$ and we fixed the RIS panel at position $(20\text{m}, 8\text{m})$. By analyzing this figure, it is possible to observe curves for five different configurations. The parameters used to draw the comparison on UMT scenario are: $N_{tx}=64$, $N_s=3$, $N_{rx}=16$, $N_{ris}=144$ or 576 elements, and $N_c=1$. Curves with the proposed AM-SVD-APG algorithm are presented and assume the existence of direct and indirect links between transmitter and receiver. To compare with our algorithm, we include results obtained with the APG algorithm from [12], and with the well-known PGM algorithm from [32]. While the curves of the RIS aided communication links are always better than the conventional case without RIS, the best BER performance is achieved with AM-SVD-APG algorithm, with higher gains obtained when using a larger number of RIS elements.

By considering the same base configuration, we also present the BER versus transmitted power allocated to a user (i.e. P_{user}) in Figure 7 considering various positions of the RIS panel. In order to better understand the impact of the RIS, we divide these results into two figures, one with only 144, and the other with 576 RIS elements. The UE was placed at a fixed position of $(55, 0)\text{ m}$. On the top image of Figure 7, we can observe the different distances used when a RIS panel with 144 elements is placed between the transmitter and the receiver (UE). The reference curve corresponds to a link without any aid from a RIS. It can be observed that the best curve obtained with $N_{ris}=144$ corresponds to the case where the RIS is placed at $(50,5)\text{ m}$ which represents a setup where the UE is closer to the AP/BS. Another curve showing good

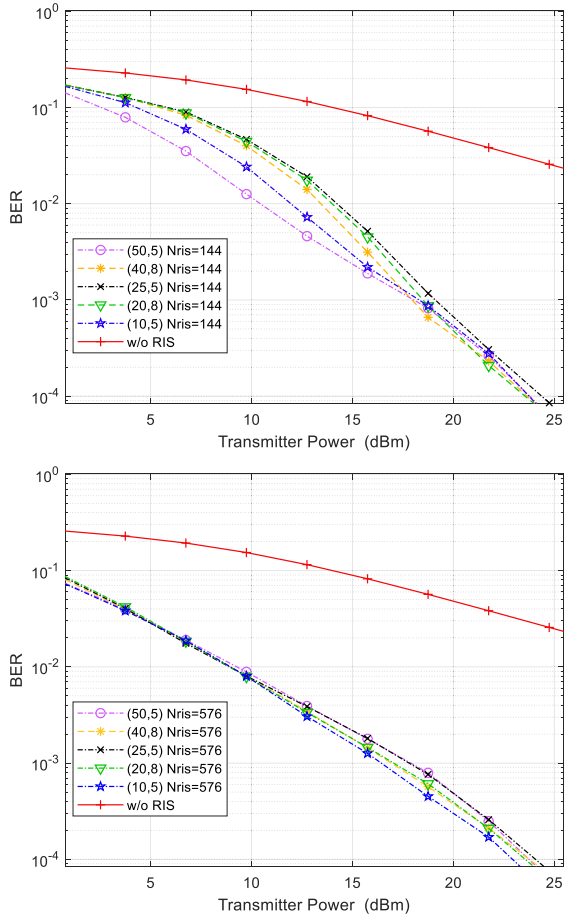


FIGURE 7. BER versus transmitted power when the receiver is fixed at (55 m, 0 m), with a configuration of $f=28\text{GHz}$, $N_{tx}=64$, $N_s=3$, $N_{rx}=16$ and $N_c=132$, but with $N_{ris}=144$ elements (top) or 576 (bottom).

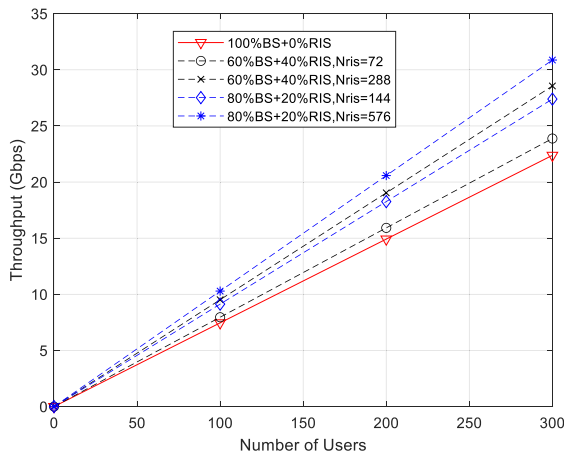


FIGURE 8. Throughput achievable with RIS in the UMT scenario, when $N_s=1$, $N_{tx}=64$, $N_{rx}=16$ and $N_c=132$.

results correspond to the case of the RIS placed at (10,5) m, i.e., close to the transmitter. As expected, the RIS panel introduces a positive impact in the communication link by decreasing the BER at the UE for the same transmitted power. When the number of RIS elements increases to $N_{ris}=576$, the performance improves, while becoming less sensitive to the placement of the RIS.

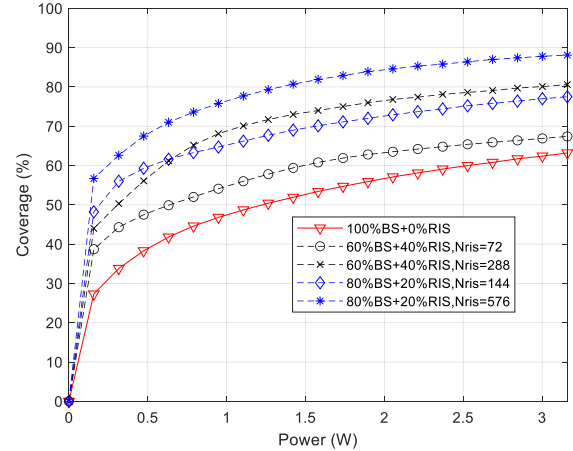


FIGURE 9. Coverage versus transmitted power with RIS in the UMT scenario, when $N_s=1$, $N_{tx}=64$, $N_{rx}=16$ and $N_c=132$.

B. SYSTEM LEVEL ANALYSIS

In the system level evaluation, we measured the overall throughput across the downlink considering a post-5G/6G RAN integrating the proposed RIS-aided scheme, as described in section IV. The main goal was to evaluate the achievable binary rate or throughput (in Gbps) versus the number of users served by both BS/AP and RIS.

To evaluate how the RIS operates in our system level scenarios, we compared a standard communication without any effect of RISs against a deployment containing RIS panels. The former consists only of direct links between the transmitters and the receivers. The other cases consist of a combination of direct link connections and RIS-aided connections. They are represented as a percentage of users that are receiving signals from the BS plus the percentage of users with RIS connections, namely as %BS + %RIS. For example, 100%BS+0%RIS, means that all users are attached to the BS, whereas 60%BS+40%RIS, represents 60% of spread out users linked to a BS only and the remaining 40% served by RIS panels also. When we consider the UMT scenario, the case 100%BSs+0%RIS assumes that the UEs are uniformly distributed within a radius of 85 m (see Figure 3 top). On the other hand, when simulating cases with BSs and RIS operating simultaneously, users that are connected to BSs will be uniformly distributed within a circle with a radius of 67 m. Moreover, the users attached to RIS panels will be uniformly distributed inside the ring defined between previous circle and a circle with a radius of 85 m (see Figure 3 middle). This means that users served by RISs are distributed across the exterior ring (RIS area) which has an area representing 38% of the total area defined by the larger 85 m radius circle.

In Figure 8, it is shown the throughput performance versus number of users in the UMT scenario. The throughput curves of Figure 8 were obtained with a maximum transmitted power of 3.16 W. It is worth mentioning that we kept most of the settings adopted in Figures 5-7. We can observe that in Figure 8, we also provide a curve representing the case without RIS. In these results we used $N_s=1$, $N_c=132$ and a RIS panel with $N_{RIS}=144$ or 576 elements. It is important to note that

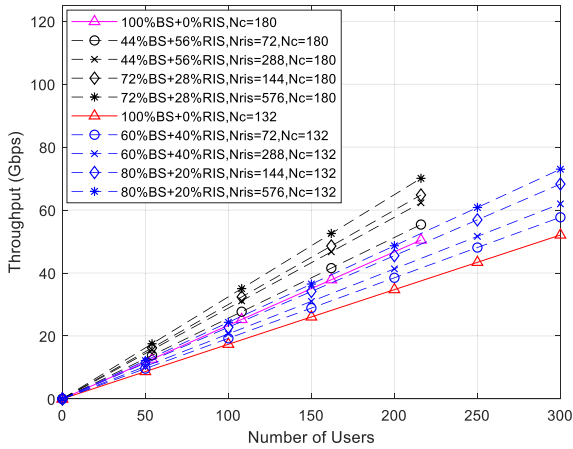


FIGURE 10. Throughput, demonstrating how RIS can affect the rate, as a function of the number of served UEs, when $N_{tx}=64$, $N_s=3$, $N_{rx}=16$. RIS are located at the same distance from nearest BS.

4 different RIS sizes appear since each RIS panel is divided into sub-panels when serving more than 1 user. Therefore, the cases of $N_{RIS}=72$ or 288 correspond to cases of 2 users being associated to a panel of 144 and 576, respectively. When the UEs are served with a direct link only (without any RIS), we have a total average throughput of approximately 22.4 Gbps for 300 users (represented as a red line). If RIS panels are added to the C-RAN, the throughput can be increased between 7% to 28% when considering a distribution of UEs of 60%BS+40%RIS, represented by black lines. Note that in this case, N_{RIS} elements correspond to half size, since two UEs have been assigned per RIS. For the other case of 80%BS+20%RIS (blue lines), the increase in throughput is between, 22% and 38%. As we observed before, we can conclude that by increasing the number of RIS elements, the communication link can be boosted. In fact, the case with $N_{RIS}=576$ elements achieve the best performance across the UEs.

Figure 9 presents the coverage versus transmitted power equivalent for the same conditions of Figure 8. The comparison between Figure 9 and Figure 8 shows that there is a direct correspondence between the throughput performance and the associated coverage. For the maximum transmitted power of 3.16 W, the smallest coverage is achieved by the case of 100%BS+0%RIS with 63% whereas the highest coverage is 88% which is obtained by the case 80%BS+20%RIS with $N_{RIS}=576$. This represents a coverage gain of 38%.

In order to provide a clear example of how RISs can impact the performance of the network, we also tested different types of configurations in the UMT scenario. For this purpose, we adopted a higher number of N_c combined with more spatial streams and larger transmit arrays.

Figure 10 presents the throughput results with this different arrangement considering a configuration of $N_{tx}=256$, $N_s=3$, $N_{rx}=16$, $N_{ris}=144$ or 576, and $N_c=132$ or 180. When we increase the number of subcarriers per user (N_c) from 132 to 180, we need to reduce the total number of users, from 300 to 216, in order to keep constant, the total

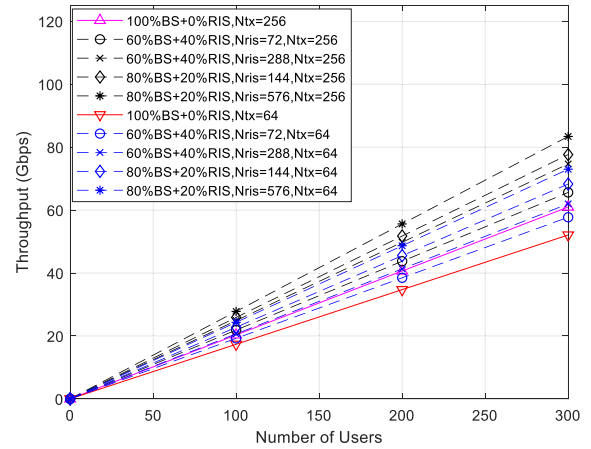


FIGURE 11. Throughput vs number of users when $N_s=3$, $N_{rx}=16$, $N_c=132$. RIS are located at the same distance from the nearest BS.

number of subcarriers with data $N_f=3300$. It is observed that the case with distribution of users 80%BS+20%RIS can achieve a gain of 40% when using $N_c=132$, and the case 72%BS+28%RIS achieves a gain 39% when using $N_c=180$. It is important to mention that these two cases ($N_c=132$ and 180) with 100%BS+0%RIS, even with a higher number of UEs connected to BSs, cannot achieve the same throughput as the cases with the aid of RIS. This behavior can be explained because UEs were spread out using a different spatial distribution from the distribution of UEs that are served only by BSs. For a fair comparison, there should be 38% of UEs attached to RIS and the remaining 62% of users attached to BSs. The curves with 60%BS+40%BS or 44%BS+56%RIS have two UEs attached to each RIS panel. They correspond to half size RIS, namely, $N_{RIS}=288$ and 72. They have a worse spatial distribution of users when compared to the case of all UEs attached to a BS. That is the reason why the performance results of $N_{RIS}=144$ are better than with $N_{RIS}=288$. Considering $N_{RIS}=288$ as reference, the throughput gain for $N_c=132$ is 19% and for $N_c=180$ is 23%. In the case of $N_{RIS}=144$, the throughput gain is 31% for $N_c=132$ and 28% for $N_c=180$. With $N_{RIS}=72$, the throughput gain is 11% for $N_c=132$ and for $N_c=180$ the gain is 10%.

From this point on, we will compare how the transmitter antenna array can affect the overall throughput of the system. In Figure 11, we evaluate the throughput using $N_c=132$ and $N_{tx}=64$ or 256 antennas but keeping the other parameters the same as in the previous case. As it was seen before, the best throughput can be achieved with the highest number of RIS elements, namely with 576 RIS elements. It can be observed that with 80%BS+20%RIS, $N_{RIS}=576$ and $N_{tx}=256$ it is possible to achieve up to 37% better performance than the standard link (100%BS+0%RIS with $N_{tx}=256$). The best case for $N_{tx}=64$, corresponds to 80%BS+20%RIS with $N_{RIS}=576$, where we observe an increase of 40% face to the 100%BS+0%RIS. The worst case for $N_{tx}=256$, corresponds to 60%BS+40%RIS with $N_{RIS}=72$, where it can be seen an increase of 11% compared to the 100%BS+0%RIS case.

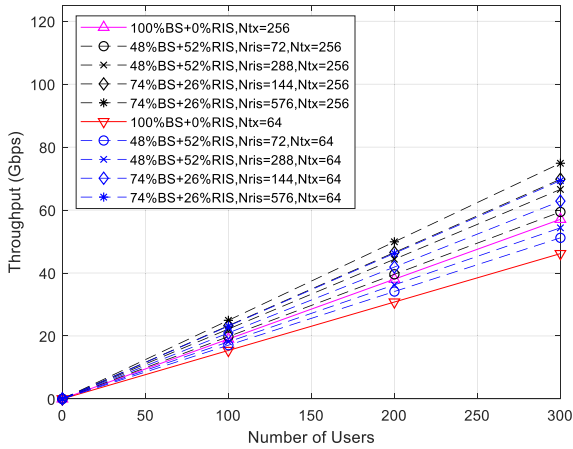


FIGURE 12. Comparison of different achievable throughput using $N_s=3$, $N_{Tx}=16$, $N_c=132$ in the UMT scenario shown on bottom image of figure 3.

Based on these results, we can expect that the proposed RIS based approach can be effective in MIMO schemes with large antenna arrays and also with RIS panels with a large number of elements. To assess this behavior, we tested the same UMT scenario but with RIS panels located at different distance from the nearest BS, as illustrated in Figure 3 (bottom image), as it is a more realistic approach to place the RIS panels.

Figure 12 shows the simulated throughput when considering the bottom scenario of Figure 3, which represents a more realistic/typical deployment. The same parameters configuration adopted in Figure 11 was used in this case, which allows us to verify that similar results were obtained. The maximum transmitted power was set as 3.16 W. There is a different spatial distribution of UEs when compared to the previous two figures. In the cases of 74%BS+26%RIS, there is a single UE attached to each RIS, and two for the cases of 48%BS+52%RIS. The latter spatial distribution of UEs is worse than the distribution of UEs for 100BS+0%RIS, while the opposite occurs for the former one. The spatial distributions that have a better uniformization are close to the cases with spatial distributions of 80%BS+20%RIS and 60%BS+40%RIS respectively. This last one is the best that has a uniform spatial distribution of UEs. The best results are achieved when using $N_{Tx}=256$ antennas, a distribution of 74%BS+26%RIS and $N_{RIS}=576$ elements. In such case, we can observe an increase of 58% over the case 100%BS+0%RIS. The worst case happens when we have $N_{Tx}=64$, which corresponds to 48%BS+56%RIS, considering $N_{RIS}=72$. In such case, we observed an increase of only 4% compared to the 100%BS+0%RIS results.

Figure 13 presents the coverage versus the total power transmitted by each BS for the same setup of Figure 12. When we compare Figure 13 with Figure 12, we observe that there is a direct correspondence between the throughput performance and the associated coverage. For the maximum transmitted power of 3.16 W with $N_{Tx}=64$, the smallest coverage is achieved in the case 100%BS+0%RIS with 43.6% whereas the highest coverage is obtained in the case of 74%BS+26%RIS and $N_{RIS}=576$ with 66.8%. This is a

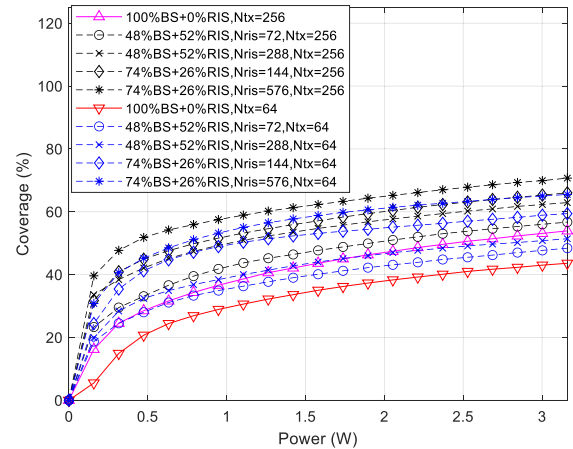


FIGURE 13. Coverage of throughput using fixed parameters as $N_s=3$, $N_{Tx}=16$, $N_c=132$, relative to the realistic UMT scenario presented in previous Figure 11.

coverage gain of 52%. Moreover, for $N_{Tx}=256$, the smallest coverage is achieved for 100%BS+0%RIS resulting in 53.9%, whereas the highest coverage is 70.7% which is obtained for 74%BS+26%RIS with $N_{RIS}=576$. This is a coverage gain of 31%. When comparing the coverage performance of Figures 9, which considers $N_s=1$, against Figure 13, which considers $N_s=3$, we observe a coverage loss of 31% as the number of spatial streams per user increases.

From this point on we will consider the IOO environment, in which all RIS are placed at a distance of 10 m from the nearest AP. To simulate the IOO scenario only with APs, we distributed uniformly the UEs within a radius of 17 m. When simulating the system with APs and RIS, the UEs that are connected to APs are uniformly distributed within a radius of 10 m, while the users attached to RIS are uniformly distributed within a radius of 7 m (see Figure 2). The area ratio of a circle with radius 10 m over another with radius 17 m is about 35%. This means that the users served by RIS panels should be 65% of the total on average. 14 shows the throughput that can be achieved with $N_c=60$, and $N_c=120$. This scenario assumes a different carrier frequency than the one considered in the UMT scenario. The system operates at 100 GHz which, due to the shorter wavelength, allows us to work with more elements at the RIS, i.e., $N_{RIS}=256$ up to 2048. It is clear that the best throughput that can be achieved in this scenario corresponds to the cases with a higher number of RIS elements, namely $N_{RIS}=2048$. We can also observe that the instance where a RIS-aided UE is attached to a dedicated RIS, with a distribution of 57%AP + 43%RIS, $N_c=60$ and $N_{RIS}=2048$, has a gain of 29% when compared to the standard link (100%AP+0%RIS). The case labeled as 14%AP + 84%RIS with $N_c=120$, $N_{RIS}=2048$, has a gain of 43% when compared to the reference 100%AP+0%RIS.

Considering the cases with $N_c=120$, we reduce the users that are attached to the AP to keep a single user per RIS. Furthermore, as we double the number of subcarriers per user, N_c , we need to reduce to half the total number of users, namely from 168 to 84, in order to keep constant, the total

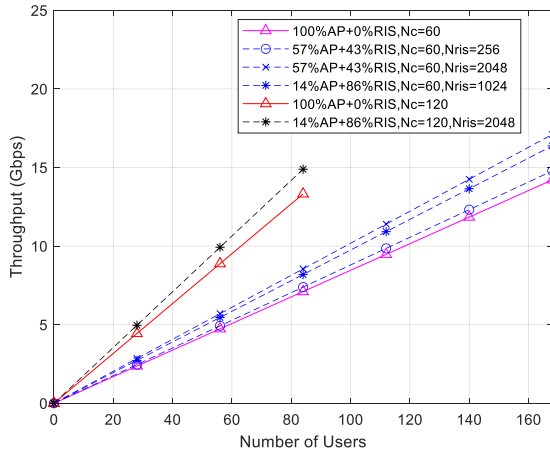


FIGURE 14. Throughput, demonstrating how RIS can affect the rate, in the IOO environment using $N_{tx}=64$, $N_s=2$, $N_{rx}=16$.

number of subcarriers allocated with data symbols ($N_f=840$). It can be observed that the case with 14%AP + 86%RIS and $N_c = 60$ can achieve higher throughputs than $N_c = 120$, for the maximum number of users served simultaneously. This is explained by the worse spatial distribution of UEs with $N_c = 120$ when compared to the distribution with $N_c = 60$. It is also important to point out that the adoption of RISs allow us to achieve throughput improvements of 24% for 14%AP+86%RIS with $N_{RIS}=1024$ and a gain of 13% when we only use 256 reflective elements (case 57%AP+43%RIS with $N_{RIS} = 256$).

VI. CONCLUSION

Due to its potential performance and implementation gains, RISs are considered a key technology for future wireless networks, in particular for post-5G and 6G systems. Within this scope, in this paper we reported system-level assessments of RIS-aided post-5G/6G RAN deployments operating at mmWave (28 GHz) and sub-THz (100 GHz) bands. Considering scenarios where the communication for different users is based on orthogonal multiple access, we first proposed an iterative algorithm for accomplishing joint precoding and RIS optimization in multicarrier point-to-point MIMO communications. Link level simulation results showed that the proposed approach can be more effective than other existing approaches for harvesting the potential gains of RIS-aided communications. This algorithm was then integrated into the system level evaluation of a post 5G/6G RAN operating with multiple BSs, RIS panels and users. The assessment was performed over two different scenarios, IOO and UMT, and considered both near-field and far-field propagation models.

Our numerical results showed that it is possible to provide large transmissions rates with the aid of RIS both in outdoor and indoor environments at mmWave and sub-THz bands. In fact, at 28 GHz the results showed improvements in the overall throughput, with gains of up to 58% over a deployment without any RIS, and coverage gains of up to 53% over the standard communication without any aid. It was thus observed that it is possible to extend the coverage from

cell/BS, and also achieves better SNR at the UEs, increasing the overall performance of the system. By increasing the number of elements in each RIS panel, it is possible to improve the results even further. Furthermore, to obtain the best throughput gains, RIS panels should be placed near the edge of the cells. However, the throughput performance seems to not degrade substantially when RIS are placed at different distances of the nearest BS/AP. As future work, we intend to extend the joint active and passive beamforming algorithm as well as the system level evaluation to multi-user downlink/uplink and multi-cell MIMO scenarios, incorporating realistic low-resolution RIS phases-shifts and imperfect channel knowledge.

APPENDIX

A. DERIVATION OF $\nabla_{\varphi^*} f(\varphi)$

To derive the complex-valued gradient $\nabla_{\varphi^*} f(\varphi)$ we adopt the procedure described in [33]. First, we write the complex differential of $f(\mathbf{F}[k], \varphi)$ with respect to φ^* as

$$df = - \sum_{k=1}^{N_c} \text{Tr} \left\{ \frac{\rho}{P_n} \left(\mathbf{I}_{N_s} + \frac{\rho}{P_n} \mathbf{F}[k]^H \mathbf{H}[k]^H \mathbf{H}[k] \mathbf{F}[k] \right)^{-1} \times \left(\mathbf{F}[k]^H \mathbf{H}[k]^H d\mathbf{H}[k] \mathbf{F}[k] + \mathbf{F}[k]^H d\mathbf{H}[k]^H \mathbf{H}[k] \mathbf{F}[k] \right) \right\} \quad (16)$$

From the total channel matrix expression (2) we can also directly obtain THE following complex differential

$$d\mathbf{H}[k] = \mathbf{H}[k]^{R,D} \text{diag}(d\varphi) \mathbf{H}[k]^{S,R} \quad (17)$$

Inserting this expression into (1) and using the following relation that is simple to verify for a generic matrix \mathbf{Z}

$$\text{Tr}\{\mathbf{Z} \text{diag}(d\varphi)\} = \text{diag}(\mathbf{Z})^T d\varphi, \quad (18)$$

we can rewrite (15) as

$$df = - \frac{\rho}{P_n} \sum_{k=1}^{N_c} \text{diag} \left[\mathbf{H}^{S,R}[k] \mathbf{F}[k] \left(\mathbf{I}_{N_s} + \frac{\rho}{P_n} \mathbf{F}[k]^H \mathbf{H}[k]^H \mathbf{H}[k] \mathbf{F}[k] \right)^{-1} \times \mathbf{H}[k] \mathbf{F}[k]^{-1} \mathbf{F}[k]^H \mathbf{H}[k]^H \mathbf{H}^{R,D}[k] \right]^T d\varphi_i - \frac{\rho}{P_n} \sum_{k=1}^{N_c} \times \text{diag} \left[\mathbf{H}^{R,D}[k]^H \mathbf{H}[k] \mathbf{F}[k] \times \left(\mathbf{I}_{N_s} + \frac{\rho}{P_n} \mathbf{F}[k]^H \mathbf{H}[k]^H \mathbf{H}[k] \mathbf{F}[k] \right)^{-1} \mathbf{F}[k]^H \mathbf{H}^{S,D}[k]^H \right]^T d\varphi_i^* \quad (19)$$

Then using table 3.2 from [33] results in following gradient expression

$$\nabla_{\varphi^*} f(\varphi) = - \frac{\rho}{P_n} \sum_{k=1}^{N_c} \text{diag} \left[\left(\mathbf{H}[k]^{R,D} \right)^H \mathbf{H}[k] \mathbf{F}[k] \right]$$

$$\begin{aligned} & \times \left(\mathbf{I}_{N_s} + \frac{\rho}{P_n} \mathbf{F}[k]^H \mathbf{H}[k]^H \mathbf{H}[k] \mathbf{F}[k] \right)^{-1} \\ & \times \mathbf{F}[k]^H \left(\mathbf{H}[k]^{S,R} \right)^H \end{aligned} \quad (20)$$

which corresponds to the equation (11).

REFERENCES

- [1] M. Chafii, L. Bariah, S. Muhaidat, and M. Debbah, "Twelve scientific challenges for 6G: Rethinking the foundations of communications theory," 2022, *arXiv:2207.01843*, doi: 10.48550/arXiv.2207.01843.
- [2] V. R. J. Velez, J. P. C. B. B. Pavia, N. M. B. Souto, P. J. A. Sebastião, and A. M. C. Correia, "A generalized space-frequency index modulation scheme for downlink MIMO transmissions with improved diversity," *IEEE Access*, vol. 9, pp. 118996–119009, 2021, doi: 10.1109/ACCESS.2021.3106547.
- [3] S. Basharat, M. Khan, M. Iqbal, U. S. Hashmi, S. A. R. Zaidi, and I. Robertson, "Exploring reconfigurable intelligent surfaces for 6G: State-of-the-art and the road ahead," *IET Commun.*, vol. 16, no. 13, pp. 1458–1474, Aug. 2022, doi: 10.1049/cmu.2.12364.
- [4] E. Basar, "Transmission through large intelligent surfaces: A new frontier in wireless communications," in *Proc. Eur. Conf. Netw. Commun. (EuCNC)*, Jun. 2019, pp. 112–117, doi: 10.1109/EuCNC.2019.8801961.
- [5] E. Björnson, Ö. Özdogan, and E. G. Larsson, "Reconfigurable intelligent surfaces: Three myths and two critical questions," *IEEE Commun. Mag.*, vol. 58, no. 12, pp. 90–96, Dec. 2020, doi: 10.1109/MCOM.001.2000407.
- [6] E. Björnson, H. Wymeersch, B. Matthiesen, P. Popovski, L. Sanguinetti, and E. de Carvalho, "Reconfigurable intelligent surfaces: A signal processing perspective with wireless applications," *IEEE Signal Process. Mag.*, vol. 39, no. 2, pp. 135–158, Mar. 2022, doi: 10.1109/MSP.2021.3130549.
- [7] F. Yang, P. Pitchappa, and N. Wang, "Terahertz reconfigurable intelligent surfaces (RISs) for 6G communication links," *Micromachines*, vol. 13, no. 2, p. 285, Feb. 2022, doi: 10.3390/mi13020285.
- [8] H. Zhang, B. Di, L. Song, and Z. Han, "Reconfigurable intelligent surfaces assisted communications with limited phase shifts: How many phase shifts are enough?" *IEEE Trans. Veh. Technol.*, vol. 69, no. 4, pp. 4498–4502, Apr. 2020, doi: 10.1109/TVT.2020.2973073.
- [9] S. Zeng, H. Zhang, B. Di, Z. Han, and L. Song, "Reconfigurable intelligent surface (RIS) assisted wireless coverage extension: RIS orientation and location optimization," *IEEE Commun. Lett.*, vol. 25, no. 1, pp. 269–273, Jan. 2021, doi: 10.1109/LCOMM.2020.3025345.
- [10] M. A. ElMossallamy, H. Zhang, L. Song, K. G. Seddik, Z. Han, and G. Y. Li, "Reconfigurable intelligent surfaces for wireless communications: Principles, challenges, and opportunities," *IEEE Trans. Cognit. Commun. Netw.*, vol. 6, no. 3, pp. 990–1002, Sep. 2020, doi: 10.1109/TCCN.2020.2992604.
- [11] C. Huang, G. C. Alexandropoulos, C. Yuen, and M. Debbah, "Indoor signal focusing with deep learning designed reconfigurable intelligent surfaces," in *Proc. IEEE 20th Int. Workshop Signal Process. Adv. Wireless Commun. (SPAWC)*, Jul. 2019, pp. 1–5, doi: 10.1109/SPAWC.2019.8815412.
- [12] J. Praia, J. P. Pavia, N. Souto, and M. Ribeiro, "Phase shift optimization algorithm for achievable rate maximization in reconfigurable intelligent surface-assisted THz communications," *Electronics*, vol. 11, no. 1, p. 18, Dec. 2021, doi: 10.3390/electronics11010018.
- [13] S. Zhang and R. Zhang, "Capacity characterization for intelligent reflecting surface aided MIMO communication," *IEEE J. Sel. Areas Commun.*, vol. 38, no. 8, pp. 1823–1838, Aug. 2020, doi: 10.1109/JSAC.2020.3000814.
- [14] C. Huang, G. C. Alexandropoulos, A. Zappone, M. Debbah, and C. Yuen, "Energy efficient multi-user MISO communication using low resolution large intelligent surfaces," in *Proc. IEEE Globecom Workshops (GC Wkshps)*, Dec. 2018, pp. 1–6, doi: 10.1109/GLOCOMW.2018.8644519.
- [15] X. Mu, Y. Liu, L. Guo, J. Lin, and N. Al-Dhahir, "Capacity and optimal resource allocation for IRS-assisted multi-user communication systems," *IEEE Trans. Commun.*, vol. 69, no. 6, pp. 3771–3786, Jun. 2021, doi: 10.1109/TCOMM.2021.3062651.
- [16] J. P. Pavia, V. Velez, R. Ferreira, N. Souto, M. Ribeiro, J. Silva, and R. Dinis, "Low complexity hybrid precoding designs for multiuser mmWave/THz ultra massive MIMO systems," *Sensors*, vol. 21, no. 18, p. 6054, Sep. 2021, doi: 10.3390/s21186054.
- [17] X. Pei, H. Yin, L. Tan, L. Cao, Z. Li, K. Wang, K. Zhang, and E. Björnson, "RIS-aided wireless communications: Prototyping, adaptive beamforming, and indoor/outdoor field trials," *IEEE Trans. Commun.*, vol. 69, no. 12, pp. 8627–8640, Dec. 2021, doi: 10.1109/TCOMM.2021.3116151.
- [18] S. Liu, P. Ni, R. Liu, Y. Liu, M. Li, and Q. Liu, "BS-RIS-user association and beamforming designs for RIS-aided cellular networks," in *Proc. IEEE/CIC Int. Conf. Commun. China (ICCC)*, Jul. 2021, pp. 563–568, doi: 10.1109/ICCC52777.2021.9580193.
- [19] B. Sahlbom, M. I. Poulakis, and M. D. Renzo, "Reconfigurable intelligent surfaces: Performance assessment through a system-level simulator," *IEEE Wireless Commun.*, early access, Aug. 8, 2022, doi: 10.1109/MWC.015.2100668.
- [20] Q. Gu, D. Wu, X. Su, H. Wang, J. Cui, and Y. Yuan, "System-level simulation of reconfigurable intelligent surface assisted wireless communications system," 2022, *arXiv:2206.14777*, doi: doi.org/10.48550/arXiv.2206.14777.
- [21] E. Telatar, "Capacity of multi-antenna Gaussian channels," *Eur. Trans. Telecommun.*, vol. 10, no. 6, pp. 585–595, Nov. 1999.
- [22] A. Goldsmith, S. A. Jafar, N. Jindal, and S. Vishwanath, "Capacity limits of MIMO channels," *IEEE J. Sel. Areas Commun.*, vol. 21, no. 5, pp. 684–702, Jun. 2003, doi: 10.1109/JSAC.2003.810294.
- [23] N. Parikh and S. Boyd, "Proximal algorithms," *Found. Trends Optim.*, vol. 1, no. 3, pp. 123–231, Nov. 2014.
- [24] A. Beck, *First-Order Methods in Optimization* (MOS-SIAM Series on Optimization). Philadelphia, PA, USA: SIAM, 2017.
- [25] 5G—Study on Channel Model for Frequencies From 0.5 to 100 GHz, document TR 38.901 V.16.1.0, 3GPP, Nov. 2020.
- [26] F. Bohagen, P. Orten, and G. Oien, "On spherical vs. plane wave modeling of line-of-sight MIMO channels," *IEEE Trans. Commun.*, vol. 57, no. 3, pp. 841–849, Mar. 2009, doi: 10.1109/TCOMM.2009.03.070062.
- [27] K. Dovelos, S. D. Assimonis, H. Quoc Ngo, B. Bellalta, and M. Matthaiou, "Intelligent reflecting surfaces at terahertz bands: Channel modeling and analysis," in *Proc. IEEE Int. Conf. Commun. Workshops (ICC Workshops)*, Montreal, QC, Canada, Jun. 2021, pp. 1–6, doi: 10.1109/ICCWkshps50388.2021.9473890.
- [28] J. M. Jornet and I. F. Akyildiz, "Channel modeling and capacity analysis for electromagnetic wireless nanonetworks in the terahertz band," *IEEE Trans. Wireless Commun.*, vol. 10, no. 10, pp. 3211–3221, Oct. 2011, doi: 10.1109/TWC.2011.081011.100545.
- [29] C. Balanis, *Antenna Theory*. Hoboken, NJ, USA: Wiley, 1997.
- [30] J. Huang, C. Wang, Y. Sun, R. Feng, J. Huang, B. Guo, Z. Zhong, and T. J. Cui, "Reconfigurable intelligent surfaces: Channel characterization and modeling," *Proc. IEEE*, vol. 110, no. 9, pp. 1290–1311, Sep. 2022, doi: 10.1109/JPROC.2022.3186087.
- [31] NR; Physical Layer; General Description, document TS 38.201, 3GPP, Release 17, 2021.
- [32] N. S. Perovic, L. Tran, M. Di Renzo, and M. F. Flanagan, "Achievable rate optimization for MIMO systems with reconfigurable intelligent surfaces," *IEEE Trans. Wireless Commun.*, vol. 20, no. 6, pp. 3865–3882, Jun. 2021, doi: 10.1109/TWC.2021.3054121.
- [33] A. Hjørungnes, *Complex-Valued Matrix Derivatives With Applications in Signal Processing and Communications*. Cambridge, U.K.: Cambridge Univ. Press, 2011.



VASCO R. J. VELEZ received the B.Sc. and M.Sc. degrees in telecommunications and computer engineering from ISCTE-IUL, in 2016 and 2018, respectively. He is currently pursuing the Ph.D. degree in information science and technology for effective RF techniques against unauthorized UAVs for his thesis. In 2017, he joined Instituto de Telecomunicações (IT) as part of his M.Sc. thesis, he worked in the spoofing of GNSS signals. His research interests include the development of new technologies for communications systems, wireless networks, signal processing for telecommunications, MIMO schemes, MIMO radar, source localization, GNSS signals, and unmanned aerial vehicles.



JOÃO PEDRO C. B. B. PAVIA received the Ph.D. degree in information science and technology from the University Institute of Lisbon (ISCTE), in 2022. At his early stage research career, he worked for an international project funded by FCT and TUBITAK aiming to understand the interaction between glow discharge detectors and THz waves in order to develop a new generation of imaging systems for security applications. He was also involved as a local organizer

in several conferences and symposiums promoted by ISCTE and Instituto de Telecomunicações (IT). He is currently an Assistant Professor with Universidade Lusófona and a Researcher with COPELABS and IT. His research interests include the development of new technologies for the terahertz band, wireless communication networks, signal processing, MIMO schemes, metamaterials, big data, machine learning, and cybersecurity. He is also a member of COST - European Cooperation in Science and Technology, being part of the working group COST CA20120 INTERACT which as the purpose to develop intelligence-enabling radio communications for seamless inclusive interactions. He serves as a reviewer for journals of Multidisciplinary Digital Publishing Institute (MDPI) and he was also a reviewer of the IEEE Vehicular Technology Conference: VTC2021-Fall, VTC2022 Spring, and VTC2023-Spring.



NUNO M. B. SOUTO (Senior Member, IEEE) received the Graduate degree in aerospace engineering-avionics branch from Instituto Superior Técnico, Lisbon, Portugal, in 2000, and the Ph.D. degree, in 2006. From November 2000 to January 2002, he was a Researcher in automatic speech recognition with Instituto de Engenharia e Sistemas de Computadores, Lisbon. He joined the University Institute of Lisbon (ISCTE) as an Assistant Professor, in 2006. He has been a

Researcher with Instituto de Telecomunicações (IT), Portugal, since 2002, and has been involved in several international research projects and many national projects. His research interests include wireless networks, signal processing for communications, OFDM, single carrier transmission with frequency domain equalization, channel estimation, synchronization, MIMO schemes, wireless sensor networks, and unmanned aerial vehicles. He is a member of the IEEE Signal Processing Society.



PEDRO J. A. SEBASTIÃO (Member, IEEE) received the Ph.D. degree in electrical and computer engineering from IST. He is currently a Professor with the Information Science and Technology Department, ISCTE-IUL. He is also the Board Director of the AUDAX-ISCTE-Entrepreneurship and Innovation Center, ISCTE, responsible for the LABS LISBOA incubator and a Researcher with the Institute of Telecommunications. He has oriented several master's dissertations and Ph.D. theses. He is the author or coauthor of more than 200 scientific articles and he has been responsible for several national and international research and development projects. He has been an expert and an evaluator of more than 100 national and international civil and defense research and development projects. It has several scientific, engineering, and pedagogical awards. Also, he has organized or co-organized more than 50 national and international scientific conferences. He planned and developed several postgraduate courses in technologies and management, entrepreneurship and innovation, and the transfer of technology and innovation. He has supported several projects involving technology transfer and creation of start-ups and spin offs of value to society and market. He has developed his professional activity in the National Defense Industries, initially in the Office of Studies and later as the Board Director of the Quality Department of the Production of New Products and Technologies. He was also responsible for systems of communications technology in the Nokia-Siemens business area. His research interests include monitoring, the control and communications of drones, unnamed vehicles, planning tools, stochastic process (modeling and efficient simulations), the Internet of Things, and efficient communication systems.

Since December 2007, he has been a Full Professor with ISCTE, Lisbon University Institute, Portugal. He has been a Researcher with Instituto de Telecomunicações (IT), Portugal, since 1992. He was a Postgraduate Researcher with RWTH, Aachen, Germany, from October 1994 to September 1995. He visited the Nokia Research Center, from September to December 1998, as a Visiting Scientist. From September 2000 to August 2001, he joined Ericsson Eurolab, The Netherlands. His research interests include CDMA, OFDMA, NOMA, MIMO, radio resource management, broadcasting technology, and enhanced multimedia broadcast/multicast services. He is a member of Communications Society of IEEE and has been a member of "Ordem dos Engenheiros," since 1987.



AMÉRICO M. C. CORREIA (Senior Member, IEEE) received the B.Sc. degree in electrical engineering from the University of Angola, in 1983, and the M.Sc. and Ph.D. degrees in telecommunications from Instituto Superior Técnico (IST), Lisbon, Portugal, in 1990 and 1994, respectively. From 1991 to 1999, he was with IST as an Assistant Professor. From August 2000 to November 2007, he was an Associate Professor with ISCTE. Since December 2007, he has been a Full Professor with ISCTE, Lisbon University Institute, Portugal. He has been a

Researcher with Instituto de Telecomunicações (IT), Portugal, since 1992. He was a Postgraduate Researcher with RWTH, Aachen, Germany, from October 1994 to September 1995. He visited the Nokia Research Center, from September to December 1998, as a Visiting Scientist. From September 2000 to August 2001, he joined Ericsson Eurolab, The Netherlands. His research interests include CDMA, OFDMA, NOMA, MIMO, radio resource management, broadcasting technology, and enhanced multimedia broadcast/multicast services. He is a member of Communications Society of IEEE and has been a member of "Ordem dos Engenheiros," since 1987.

• • •